Comparison of scanning strategies in UAV-mounted multichannel GPR-SAR systems using antenna arrays

M. García-Fernández, *Member, IEEE*, G. Álvarez-Narciandi, *Member, IEEE*, F. Las Heras, *Senior Member, IEEE*, Y. Álvarez-López

***Abstract*—Ground Penetrating Radar (GPR) systems on board Unmanned Aerial Vehicles (UAVs) have been successfully used for subsurface imaging applications. Their capability to detect buried targets avoiding the contact with the soil turn these systems into a great solution to detect buried threats, such as landmines and Improvised Explosive Devices (IEDs). Significant advances have been also conducted to enhance the detection capabilities of these systems, complementing the Synthetic Aperture Radar (SAR) processing methods with several clutter mitigation techniques. However, the improvement in the scanning throughput (i.e., increasing the inspected area in a given time) remains a significant challenge. In this regard, this article compares several scanning strategies for UAV-mounted multichannel GPR-SAR systems using antenna arrays. In particular, two different scanning strategies have been compared: a uniform scheme and a non-uniform strategy called 3X. In addition, different across-track spacing values to generate dense and sparse sampling distributions were considered for each scanning scheme. After conducting a theoretical analysis of these strategies, they have been experimentally validated with measurements gathered with a portable scanner and during flights in realistic scenarios. Results show that the dense configurations of both scanning strategies yield good quality images of buried targets while improving the scanning throughput (compared to a single-channel architecture). In particular, the dense uniform scheme (with a 20 cm across-track spacing) achieves a greater reduction in the inspection time, compared to the dense 3X strategy, at the expense of a slightly smaller signal to clutter ratio.**

***Index Terms*—Ground Penetrating Radar, Synthetic Aperture Radar, Unmanned Aerial Vehicle, multichannel radar, scanning throughput.**

María García-Fernández and Guillermo Álvarez-Narciandi are with the Centre for Wireless Innovation, Queen's University Belfast, BT7 1NN Belfast, U.K. (e-mail: m.garcia-fernandez@qub.ac.uk; g.alvarez-narciandi@qub.ac.uk).

Yuri Álvarez López and Fernando Las-Heras are with the Department of Electrical Engineering, University of Oviedo, 33203 Gijón, Spain (e-mail: alvarezyuri@uniovi.es; flasheras@uniovi.es).

This work was supported in part by the Ministry of Defense – Government of Spain and by the University of Oviedo under Contract 2019/SP03390102/00000204 / CN-19-002 ("SAFEDRONE"); in part by the MCIN/AEI/10.13039/501100011033/FEDER, UE, under Project PID2021-122697OB-I00; in part by the UK Research and Innovation (UKRI) Postdoctoral Fellowship Guarantee for Marie Skłodowska-Curie Actions (MSCA) Postdoctoral Fellowship under Project EP/X022943/1 and Project EP/X022951/1; in part by the Gobierno del Principado de Asturias/FEDER under Grant AYUD/2021/51706; and in part by the University of Oviedo under Contract PN-S 2020/49.

Manuscript received XX, 2023; revised XX, 2023.

I. Introduction

In the last few years, the development of Ground Penetrating Radar (GPR) systems mounted on board Unmanned Aerial Vehicles (UAVs) has become a trendy research topic [1]. These kinds of systems bring together the advantages of GPR (remote detection of buried targets, both metallic and non-metallic [2]) and UAVs (contactless inspection of difficult to access areas). As a result, these systems are particularly useful for detecting landmines and Improvised Explosive Devices (IEDs) as they allow a fast inspection of the subsurface while keeping a safety distance to avoid accidental detonations [3]–[7]. Furthermore, they have been also successfully used for other applications, such as measurements of soil moisture [8] or snowpack thickness [9].

In the field of buried threats detection, the ultimate goal of UAV-mounted GPR systems is to provide a high-resolution radar image of the subsurface where the hidden targets can be distinguished. To retrieve such image, the radar measurements gathered with these systems are coherently combined using a Synthetic Aperture Radar (SAR) algorithm [10], [11] or solving a linear inverse scattering problem [12], [13]. In turn, this requires that the measurements are geo-referred with cm-level accuracy. This challenge has been mainly overcome by integrating a Real Time Kinematic (RTK) system on board the UAV, as proposed in [3].

Several prototypes of UAV-mounted GPR systems have been already developed for the detection of buried targets, and some of them have been successfully tested in different scenarios. After demonstrating the capability of these prototypes to detect buried threats, research efforts have been mainly devoted to improving the probability of detection and/or the quality of the retrieved images [14]. In this sense, in [15], a method called co-registration has been proposed to achieve a better focused radar image. Furthermore, to improve the signal to noise ratio, a clutter mitigation technique called distance-based Singular Value Decomposition (SVD) filtering is also applied to the measurements gathered with a UAV-mounted GPR prototype [15]. Another example of improvements in the image quality is presented in [16], where authors retrieve a model of the soil surface using interferometry and this model is then used as input in the GPR-SAR processing to improve the image focusing.

It is thus timely to face the challenge of increasing the

scanning throughput of UAV-mounted GPR systems (that is, the area inspected in a given time) without jeopardizing their detection capabilities. To this end, the use of antenna arrays has been explored in the context of GPR systems mounted on large terrestrial vehicles. For instance, in [17] 3 TX-RX antenna pairs and 3 VNAs are mounted on a truck to detect landmines, and an arrangement consisting of 6 logarithmic periodic antennas elevated with a lifter mounted on a truck was considered in [18]–[20] for humanitarian demining. Another example is also shown in [21], where 31 TX-RX antenna pairs and a GPR are placed on a quad bike for non-destructive evaluation applications. In [22], the authors propose a system composed by 8 pairs of antennas to be mounted in a vehicle for roadway and utility monitoring applications. However, the implementation of this kind of solution on a UAV-based system is not straightforward due to the additional challenges of these systems. In particular, the weight and size of the payload that can be mounted on board a UAV are heavily constrained. This means that it is significantly difficult to integrate multiple relatively large antennas. Some other challenges are the fact that UAV-mounted GPR systems offer reduced dynamic range compared to ground-based GPR systems as the antennas are not in contact with the soil, and that they yield irregular acquisition grids, among others. The first UAV-based prototypes employing more than one RX antenna have been presented in [23] (performing 3D scanning with 1 TX and 2 RX) and in [24] (performing a single forward-backward sweep with 1 TX and 3 RX). A multichannel UAV-mounted GPR-SAR system was recently presented in [25]. However, the integration of antenna arrays on board UAV-mounted GPR systems is still a heavily understudied research topic.

The scope of this article is to analyze different scanning strategies for a multichannel UAV-mounted GPR-SAR system in terms of scanning throughput and detection capabilities. In particular, this study aims to test scanning strategies which provide a trade-off between the inspection time and the desired detection performance. For that purpose, the same antenna array configuration employed in [25], which comprises 3 TX and 4 RX antennas integrated into a UAV, is considered. In particular, two scanning strategies are compared by means of theoretical analysis, measurements in a controlled environment, as well as measurements of the actual UAV-mounted multichannel GPR-SAR system. The first strategy is based on a uniform scheme, whilst the second relies on a non-uniform flight path strategy called $3X$. The influence of the UAV navigation and the flight path in free-space passive UAV-mounted radar imaging has been studied in the literature [26], [27]. However, the performance of multichannel UAV-mounted GPR-SAR systems when using different scanning strategies (i.e., flight paths) has not been yet analyzed.

The article is structured as follows. Section II describes the system architecture of the UAV-mounted array-based GPR-SAR system, the methodology used to process the measurements, and the scanning strategies that have been compared (the uniform and the $3X$ schemes). A conceptual analysis and an initial validation of the $3X$ scheme are performed in Section III, whereas Section IV includes a theoretical comparison of both scanning schemes. The experimental validation has been conducted in two stages: first, ground tests have been done using a portable scanner (presented in Section V) and, then, realistic flight tests have been performed (shown in Section VI). Finally, the main conclusions are drawn in Section VII.

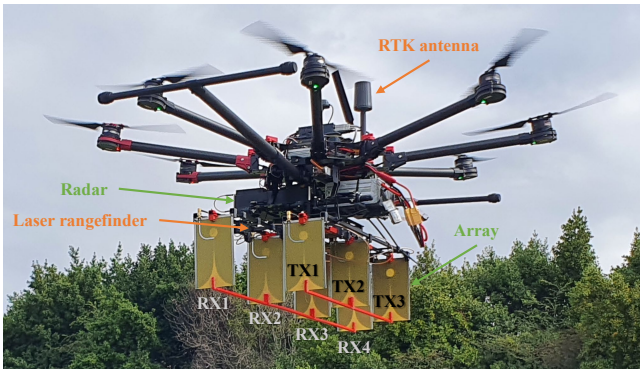

Fig. 1. Prototype of the UAV-mounted array-based GPR-SAR system.

II. System Description and Methodology

A. System description

The UAV-mounted array-based GPR-SAR system is shown in Fig. 1. Its architecture is based on that used in the single-channel prototypes [3], [28], [29]. As most commercial UAVs, it includes the following subsystems: a flight controller; common positioning sensors on board UAVs (in particular, Inertial Measurement Units (IMUs), a compass, a barometer, and a conventional Global Navigation Satellite System (GNSS) receiver); and a communication subsystem. Furthermore, in order to enable GPR-SAR processing there are two additional subsystems: the high-accuracy positioning subsystem and the radar subsystem (highlighted in Fig. 1 in orange and green, respectively). The former comprises a multi-band multi-constellation RTK receiver (to achieve cm-level positioning accuracy) and a laser rangefinder (to measure the distance to the ground). The radar subsystem is in turn composed by a dual-channel ultra-wide-band (UWB) radar module (which transmits a pseudorandom signal and operates within a frequency range from 100 MHz to 6 GHz) and the antenna array. The design and initial assembly of the antenna array were conducted by the research group Teoría do Sinal e Comunicacions, Universidade de Vigo, and they are not within the scope of this article. A preliminary study about an array of antennas to be mounted on a UAV for GPR has been presented in [30].

The antenna array is formed by two sub-arrays: one for transmission (with 3 Vivaldi antennas and a switch), and another for reception (with 4 Vivaldi antennas and another switch). This results in $3\,\text{TX} \times 4\,\text{RX} = 12\,\text{TX-RX}$ acquisition channels. This multichannel architecture (3 TX – 4 RX) allows to increase the scanning throughput and the spatial diversity. The latter means that the different transmitters illuminate the targets from different angles and this, together with the use of multiple receivers, enable to view the targets from different look angles. On the other hand, conventional architectures (with 1 TX and 1-2 RX, such as [31]) can employ antennas

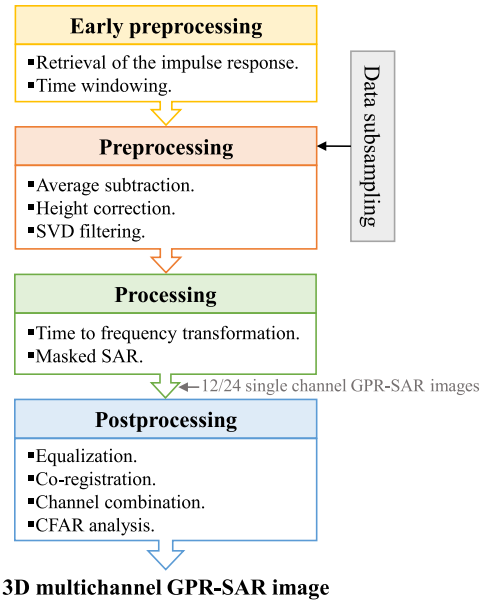

Fig. 2. Flowchart of the methodology.

working at lower frequencies (as they are usually heavier and bulkier), which could be needed for inspecting soils with higher losses (at the expense of increased inspection time).

The antenna array switching sequence, taking into account that the RX switch is a dual two-port switch and the radar module has two receiving channels, comprises the following six steps: i) TX1-RX1,RX3, ii) TX2-RX1,RX3, iii) TX3-RX1,RX3, iv) TX1-RX2,RX4, v) TX2-RX2,RX4, and vi) TX3-RX2,RX4. The frequency band of the selected antennas ranges from approximately 1 GHz up to 6 GHz [31]. However, as the penetration losses increase significantly with frequency, only the frequency band from 1 GHz to 3 GHz is used for processing. With the adopted configuration, the full acquisition of the 12 channels takes 280 ms. Assuming the UAV moves at 50 cm/s, this implies that a full acquisition is gathered every 14 cm (along-track), whereas a single measurement (of two channels) is acquired every 2.33 cm. The scanning strategy must ensure that the full observation domain is sampled fulfilling the Nyquist criterion in both along-track and across-track directions (y-axis and x-axis, respectively) [32].

B. Methodology

The prototype is configured to autonomously fly over the region of interest, following a predefined flight path. As in previous prototypes [23], [29], [33], the system sends the geo-referred radar measurements to the ground control station in real-time. In this case, the header of each radar measurement also includes a field to identify the active channel combination (i.e., the TX and the RX antenna).

Radar measurements are processed to retrieve a 3D GPR-SAR image of the inspected scenario according to the flowchart shown in Fig. 2. This methodology, which has been successfully applied for UAV-mounted GPR-SAR systems [15], [29], is composed of four main blocks:

- *Early preprocessing* (applied to each radar measurement independently). It consists of computing the impulse response (as the radar transmits a pseudo-random sequence) and performing a time window.
- *Preprocessing* (applied to all radar measurements from the same channel). This block, which mainly aims to mitigate clutter, includes average subtraction, height correction and distance-based Singular Value Decomposition (SVD) filtering [15]. It should be noted that clutter mitigation techniques are essential to detect buried targets and to improve the quality of the retrieved images. Although there are several sources of clutter in GPR scenarios, the major contributions are usually the strong reflections coming from the air-soil interface [34].
- *Processing* (also applied to all measurements from the same channel). After transforming the data from time to frequency domain, measurements are coherently combined by applying a technique called masked SAR. Masked SAR is a variation of the Delay and Sum (DAS) algorithm, initially proposed in [23], which restricts the measurements that are considered for the computation of the reflectivity at each given point to those in its vicinity (i.e., within a region, called mask, centered at the point whose reflectivity is being computed). The size of the mask is selected based on different factors, such as the area that is illuminated by the main beamwidth of the antennas and the positioning accuracy. For these studies, the size of the implemented mask is $L_{along-track} = 2\,\text{m}$ (in agreement with the projected antenna beamwidth) times $L_{across-track} = 1\,\text{m}$. The latter limitation has been selected after observing that the positioning errors are less correlated among different sweeps. As a result, after applying masked SAR, 12 3D GPR-SAR images of the area under inspection are retrieved (one per channel, that is, considering the samples of both forward and backward along-track sweeps corresponding to each combination of TX and RX antennas). In case that co-registration is applied in the last block (postprocessing), 24 images are obtained (two per channel, one corresponding to the forward along-track sweeps and the other one to the backward ones).
- *Postprocessing*. This last step is devoted to enhancing the quality of the results. In order to improve the range resolution of the resulting images, a technique called equalization (described in [14]) has been developed. Furthermore, as previously mentioned, a method called co-registration has been also proposed to enhance the image focusing. This method consists of registering the images corresponding to the forward and the backward along-track sweeps based on their intensity [15]. After the equalization and co-registration (if performed), the images from each channel are coherently combined to retrieve the final 3D multichannel GPR-SAR image. Finally, a technique to automatically detect targets is applied to facilitate the inspection of the images to the operators. This technique is based on applying a Constant False Alarm Rate (CFAR) detector [35] to each horizontal plane of the 3D GPR-SAR image.

Furthermore, a data subsampling strategy must be adopted to compensate the non-uniform sampling, avoiding over-sampled areas and mitigating the effect of deviations from the predefined flight path. As in the case of previous prototypes, the data subsampling strategy based on conditions discussed in [36] has been used.

Taking into account the characteristics of the system, the spatial resolution of the system can be approximated by (1) for the along-track and across-track directions [32], [37] (where λ_c is the wavelength at the central frequency, L is the length of the SAR aperture length, and h is the UAV height). Therefore, considering the size of the SAR mask previously indicated, $h \approx 1.5\,\text{m}$, and $\lambda_c = 0.15\,\text{m}$, the resulting along-track and across-track resolutions are $\delta_{\text{along-track}} \approx 0.45\lambda_c \approx 6.8\,\text{cm}$ and $\delta_{\text{across-track}} \approx 0.79\lambda_c \approx 11.9\,\text{cm}$. In the z-axis (i.e., the depth), the spatial resolution depends on the bandwidth (BW) and the wave speed (v) as indicated in (2) [32], [37], where c is the light speed and ε_r the medium permittivity (i.e., the soil permittivity in case of buried targets).

$$\delta_u \approx \lambda_c \frac{\sqrt{L^2/4 + h^2}}{2L} \tag{1}$$

$$\delta_z \approx \frac{v}{2\text{BW}} = \frac{c}{2\sqrt{\varepsilon_r}\text{BW}} \approx \frac{7.5}{\sqrt{\varepsilon_r}}\,\text{cm} \tag{2}$$

C. Scanning strategies

As mentioned before, the ultimate goal of the scanning strategy is to acquire enough measurements which properly cover the whole observation domain, so that a well-focused radar image can be retrieved by applying a SAR algorithm. In this contribution, two different scanning strategies will be compared: a uniform strategy and a non-uniform scheme called $3X$. In the former, the along-track sweeps are uniformly spaced at a given across-track distance Δx throughout the whole observation domain. In the latter, the system performs three along-track sweeps separated $\lambda_{min}/2$ each, then moves a larger across-track distance ($\Delta x - \lambda_{min}$) to perform another three sweeps, and so forth. The notation U-Δx and $3X$-Δx will be used to identify each scanning strategy and the considered across-track distance Δx. A sketch of both schemes is depicted in Fig. 3.

The most straightforward approach is the uniform scanning strategy, where the along-track sweeps are separated a distance small enough to acquire measurements all over the observation domain at a sampling rate fulfilling Nyquist criterion (in the spatial domain). The other approach proposed in this contribution, called $3X$ scheme, aims at minimizing the presence of grating lobes and, as a result, generating a uniform illumination as large as possible under the physical area covered by the array.

To compare the imaging results provided by the different scanning strategies, the 3D GPR-SAR image obtained with each scheme is normalized to its maximum value and the same dynamic range is employed in the graphs. This provides a fair and meaningful comparison among the different schemes because what improves the detectability of the targets is having a higher contrast between the reflectivity level of the targets and that of the surroundings.

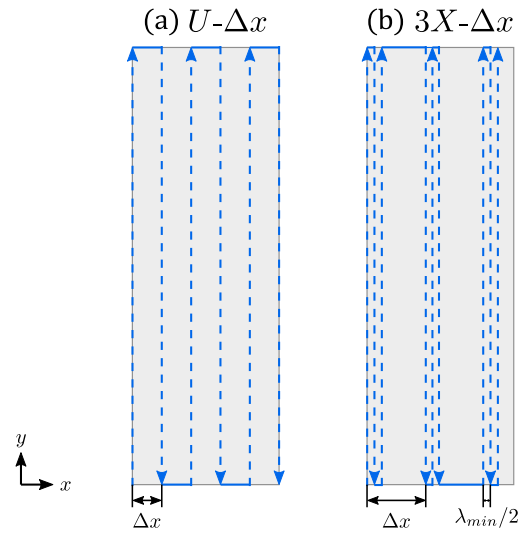

Fig. 3. Scanning strategies: (a) uniform strategy (denoted as U-Δx, where Δx is the across-track distance), and (b) $3X$ scheme (denoted as $3X$-Δx).

III. Preliminary analysis of the 3X scheme

This section aims to provide an insight into how the idea of the $3X$ scheme arose. For the application considered in this contribution, $\lambda_{min}/2$ is 5 cm, as the highest frequency used in the measurements processing is 3 GHz. However, as observed in Fig. 4(a), the across-track spacing between the antenna array elements is greater than $\lambda_{min}/2$. Therefore, the first analysis conducted upon the reception of the antenna array was devoted to characterizing the grating lobes caused by this spacing. The fields radiated by the array in the XZ plane are shown in Fig. 5. At the lowest frequency considered ($f = f_{min} = 1\,\text{GHz}$), the field below the array is significantly uniform (Fig. 5(a)), as the spacing between the antennas is $(4/9)\lambda_{max}$, that is, smaller than $\lambda_{max}/2$. However, at the highest frequency considered ($f = f_{max} = 3\,\text{GHz}$), the antenna spacing is $(4/3)\lambda_{min}$, which results in the presence of several grating lobes within the investigation domain (Fig. 5(b)).

To overcome this issue, the scanning scheme $3X$ is proposed, aiming to minimize the impact of grating lobes for the whole frequency band (from 1 GHz to 3 GHz). This scheme combines the physical aperture provided by the array with the virtual aperture achieved by moving the array in the across-track direction (i.e., in the x-axis) a distance smaller or equal than $\lambda_{min}/2 = 5\,\text{cm}$. In order to better illustrate the concept, the scheme of the physical array and the Common Mid Points (CMP) for each pair of TX-RX are depicted in Fig. 4(a). Each CMP is denoted as p_l^m, where $l = 1, 2, 3$ and $m = 1, ..., 4$ refer to the TX and the RX, respectively. Due to the symmetry of the elements, several TX-RX pairs have the same CMP (e.g., $p_2^1 = p_1^2$), resulting in 6 different CMPs, which can be denoted as p_i, $i = 1, 2, ..., 6$. It should be noted that the along-track displacement of the array (along y-axis) creates an individual path for each CMP (similarly to each individual along-track sweep of the zig-zag path of [15]).

The CMPs of the physical array are spaced 13.33 cm, which does not fulfill the Nyquist sampling rate at 3 GHz. For this goal, two virtual CMPs should be added in between. Therefore,

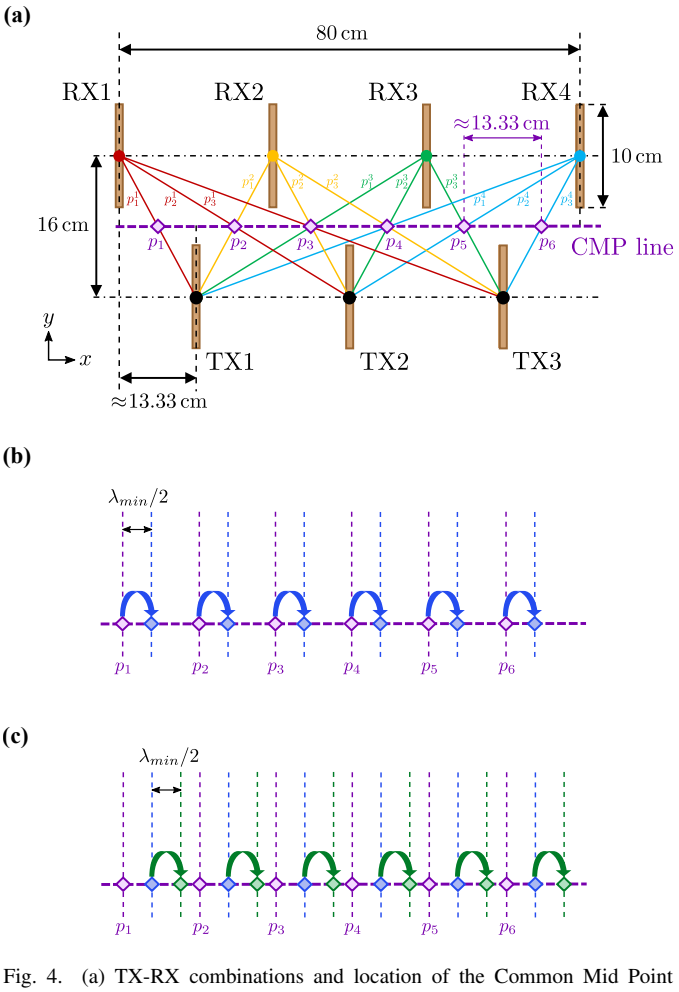

Fig. 4. (a) TX-RX combinations and location of the Common Mid Point (CMP) for each TX-RX pair. Scheme of the lateral (across-track) displacement between along-track sweeps according to the $3X$ strategy: (b) first $\lambda_{min}/2$ displacement of the array (highlighted in blue color); and (c) second $\lambda_{min}/2$ lateral shift of the array (highlighted in green color)

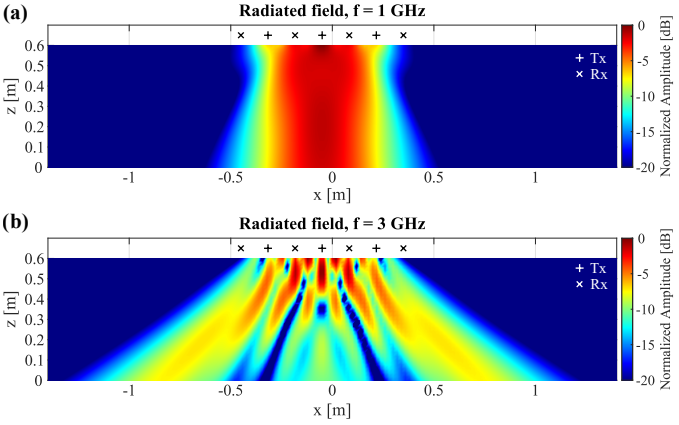

Fig. 5. Fields radiated in the XZ plane at (a) $f_{min} = 1\,\text{GHz}$, and at (b) $f_{max} = 3\,\text{GHz}$. Antenna array elements are placed along x direction, with the TX and RX elements interleaved and spaced 13.33 cm.

once a full measurement is performed, the array is displaced a small distance ($\lambda_{min}/2 = 5\,\text{cm}$) across-track (along the x-axis) to acquire another set of measurements, as shown in Fig. 4(b). Then, this procedure is repeated again, obtaining the full set of measurements shown in Fig. 4(c).

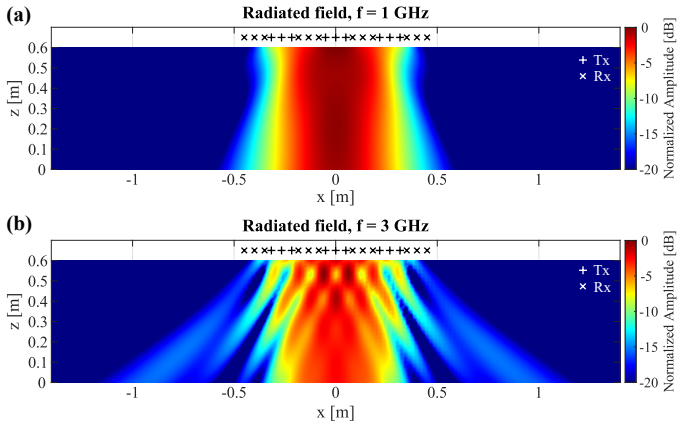

Fig. 6. Fields radiated in the XZ plane at (a) $f_{min} = 1\,\text{GHz}$, and at (b) $f_{max} = 3\,\text{GHz}$. Results corresponding to the combination of the radiated fields at three lateral positions (5 cm spacing).

Fig. 6 shows the field radiated by the array when considering the measurements acquired at three across-track positions according to the $3X$ strategy (the initial position and after two $\lambda_{min}/2 = 5\,\text{cm}$ lateral displacements, as depicted in Fig. 4(c)). Comparing Fig. 5 and Fig. 6, there are no noticeable differences at 1 GHz. However, at 3 GHz, the radiated field exhibits now a more uniform amplitude within the investigation domain (approximately for $x \in [-20, +20]$ cm) and it is not affected by the presence of grating lobes.

A. *Measurements under controlled conditions*

In order to validate the proposed scanning strategy, measurements in a controlled environment were conducted. The measurement setup is shown in Fig. 7. The radar module was placed in a plastic box and the antenna array was attached to it. This box was manually moved along two plastic tubes in one direction (y-axis, for reference purposes). For this experiment, along-track measurements were taken every 2 cm along a distance of 0.8 m. Then, once one along-track sweep was completed, the entire setup was displaced laterally (i.e., across-track) 5 cm and the second along-track sweep was conducted. Finally, another lateral displacement was performed and the third along-track sweep was acquired. As shown in Fig. 7, a metallic bar used as a reference target was placed 10 cm above the floor, tilted approximately $45°$ with respect to the x- and y- axes.

Radar measurements were coherently combined using a DAS technique [38] in the frequency range from 1 to 3 GHz (i.e., the one also used in UAV-mounted GPR experiments). Horizontal cuts (XY planes) of the retrieved radar images located at the same height as the metallic bar ($z = 0.10\,\text{m}$) obtained when considering one, two, and the three along-track sweeps of the $3X$ scheme are shown in Fig. 8. When only measurements from one along-track sweep are used (Fig. 8(a)), the metallic bar can be identified, but the resulting image is severely degraded by aliasing. If a second along-track sweep is included in the processing (Fig. 8(b)), the aliasing is noticeably reduced. Finally, with three along-track sweeps (Fig. 8(c)), the quality of the resulting image is greatly improved as this

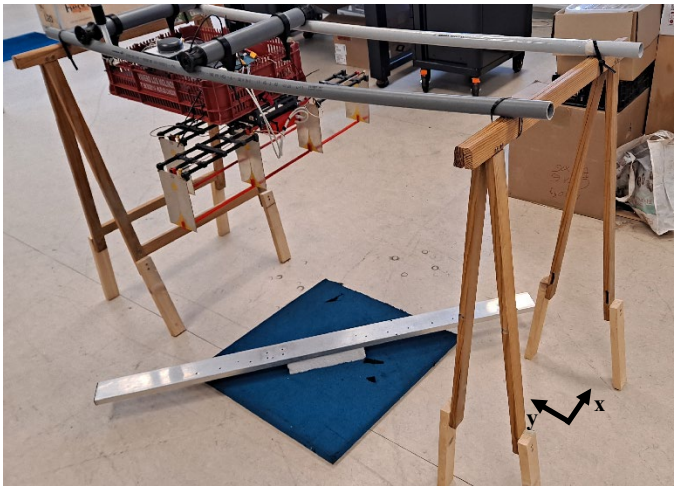

Fig. 7. Picture of the measurement setup in the laboratory. The array is attached to a plastic box containing the payload to be integrated within the UAV platform. A reference target, consisting of a tilted metallic bar, was placed at the center of the measurement domain.

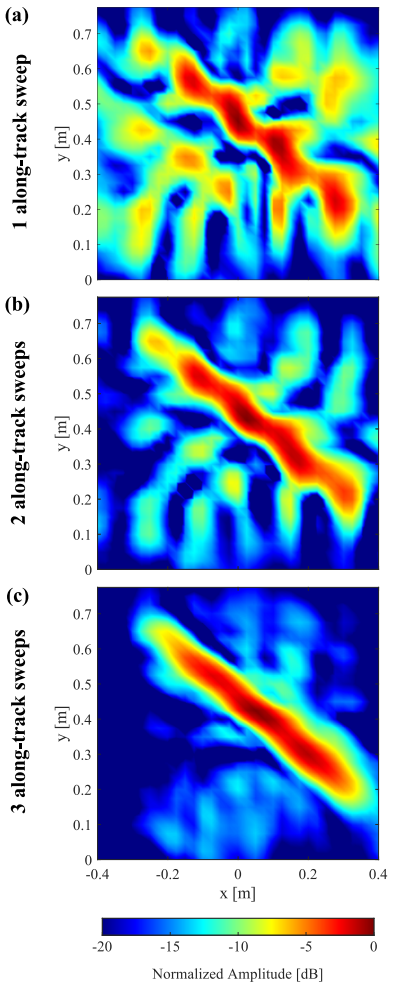

Fig. 8. Imaging results of the metallic bar using the setup shown in Fig. 7, considering: (a) a single along-track sweep, (b) two along-track sweeps, and (c) three along-track sweeps.

avoids the aliasing produced by grating lobes, and, as it can be observed, the shape of the bar is well-reconstructed.

IV. Theoretical analysis

As previously mentioned, the scanning strategy must ensure that the observation domain is properly sampled (i.e., that enough measurements are acquired). Therefore, before conducting field tests, a theoretical analysis of the distribution of the measurements acquired with the array for the different scanning strategies was performed. For this goal, the investigation domain is divided into cells, and then the number of measurements within each cell is analyzed. The size of the cells is set according to the spatial sampling intervals. For short-range radar imaging system, assuming the angle subtended by the aperture is less than the beamwidth of the antenna and the target is a point scatterer, the spatial sampling interval Δ_u must satisfy the following criterion (in along-track and across-track directions) [32], [37]:

$$\Delta_u \approx \lambda_{min} \frac{\sqrt{L^2/4 + h^2}}{2L}, \tag{3}$$

where λ_{min} is the minimum working wavelength. In practical systems the spatial sampling criterion is usually set to $\lambda_{min}/2$, as there is always a moderate distance between the aperture and the imaged scene. However, instead of considering this conventional approximation, the spatial sampling interval can be computed according to (3), taking into account that the UAV flies at $h \approx 1.5\,\text{m}$ and the size of the considered SAR mask. The resulting sampling intervals are $\Delta_{along-track} \approx 0.45\lambda_{min}$ and $\Delta_{across-track} \approx 0.79\lambda_{min}$, for the along-track and across-track directions, respectively.

Four different scanning schemes have been compared: two uniform schemes (with $\Delta x = 40\,\text{cm}$ and $\Delta x = 20\,\text{cm}$, denoted as U-40 cm and U-20 cm, respectively), and two $3X$ schemes (with $\Delta x = 80\,\text{cm}$ and $\Delta x = 40\,\text{cm}$, denoted as $3X$-80 cm and $3X$-40 cm, respectively). In this analysis, an investigation domain of $0.8\,\text{m} \times 0.8\,\text{m}$ has been considered (depicted with a black line in Fig. 9). Furthermore, it has been assumed that measurement positions are separated 2 cm along-track (note that two measurements are acquired at each position, as there are two RX channels in the radar module).

In Fig. 9(a)-(d) the positions of the array center are shown with blue squares, whereas the CMP positions (that is, the positions where measurements were taken) are shown with orange dots. The sweeps that provide measurements within the desired investigation domain are grouped with a green line in the top of each figure. To compare the performance of the different schemes, the investigation domain has been discretized in cells of $\Delta_{across-track} \times \Delta_{along-track}$ size and the number of samples falling within each cell has been computed. Furthermore, a sampling map showing the sampled cells (in yellow) and the non-sampled ones (in blue) has been also retrieved.

The number of samples per cell and the sampling maps are shown in Fig. 9(e)-(h) and Fig.9(i)-(l), respectively, for the different scanning schemes. It should be noted that the same color scale, as shown in the colorbar, is used to indicate the number of samples within each cell in Fig. 9(e)-(h) for a fair comparison between all schemes. Comparing these figures, it can be concluded that both the U-20 cm and the $3X$-40 cm

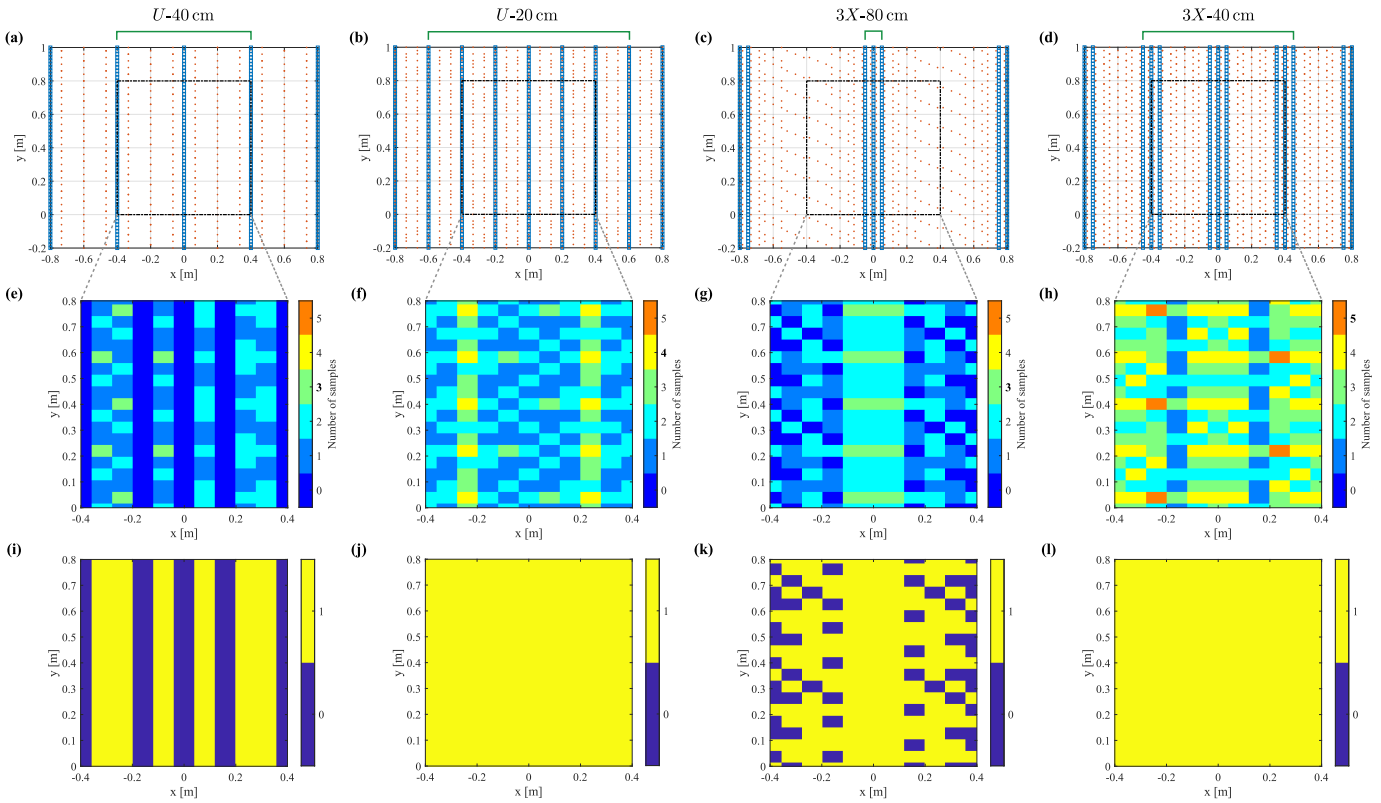

Fig. 9. Measurement positions and sampled cells for the different acquisition schemes: U-40 cm (a,e,i), U-20 cm (b,f,j), $3X$-80 cm (c,g,k) and $3X$-40 cm (d,h,l). (a-d) Investigation domain enclosed by a dashed black line, positions of the array center in blue squares, and measurement positions in orange dots. (e-h) Number of samples per cell in the investigation domain for the corresponding acquisition schemes. (i-l) Sampled cells in the investigation domain in yellow and non-sampled cells in blue.

TABLE I
MAIN STATISTICS OF THE NUMBER OF SAMPLES PER CELL, PERCENTAGE OF COVERAGE AND NUMBER OF SWEEPS REQUIRED FOR THE DIFFERENT SCANNING SCHEMES

Scheme	$U-40$cm	$U-20$cm	$3X-80$cm	$3X-40$cm
$\overline{N_s}$	0.83	1.78	1.31	2.75
σ_{N_s}	0.88	0.83	0.95	1.01
Coverage	54.55%	100%	73.21%	100%
# Sweeps	3	7	3	9

schemes provide a full coverage of the investigation domain (as shown in Fig. 9(j) and (l), respectively). With the $3X$-80 cm scheme (Fig. 9(k)) the edges of the investigation domain are not completely covered, whereas with the U-40cm (Fig. 9(i)) there are a significant number of areas without any samples.

To further compare the different schemes, a quantitative analysis is provided in Table I, showing the average and the standard deviation of the number of samples per cell ($\overline{N_s}$ and σ_{N_s}, respectively). If the measurement positions strictly fulfil the spatial sampling criterion (in both axes), the number of samples per cell would be exactly 1 (i.e., $\overline{N_s} = 1$ and $\sigma_{N_s} = 0$). It should be noted that if the sampling is significantly non-uniform, this can eventually cause a degradation in the SAR image [36] (as the oversampled areas could have high reflectivity levels even if no targets are present). The percentage of cells sampled with each scheme and the number of along-track sweeps required to cover the desired investigation domain (denoted as coverage and # sweeps in Table I) have been calculated as well.

Comparing the two schemes that provide full coverage, with the U-20 cm scheme the coverage is more uniform (as shown in Fig. 9), which is in agreement with the fact that the standard deviation of the number of samples per cell is the smallest. On the other hand, with the $3X$-40 cm scheme, there are more samples gathered all over the investigation domain (also in agreement with having the highest average number of samples per cell).

Finally, it is worth mentioning that the former scheme requires fewer along-track sweeps than the $3X$-40 cm scheme. Therefore, it is expected that with this scheme (U-20 cm) the inspection will be faster (as the same area is covered with fewer along-track sweeps, i.e., in less time) at the expense of acquiring a smaller amount of samples compared to the latter scheme ($3X$-40 cm).

V. GROUND TESTS USING A PORTABLE SCANNER

After conducting the theoretical analysis, the array was placed in the portable scanner presented in [39] to perform field tests to compare the imaging results obtained with the different scanning schemes. In this portable scanner, a plastic box containing the desired payload can be manually displaced over an area of approximately 1 m $\times$ 1 m. Besides the antenna

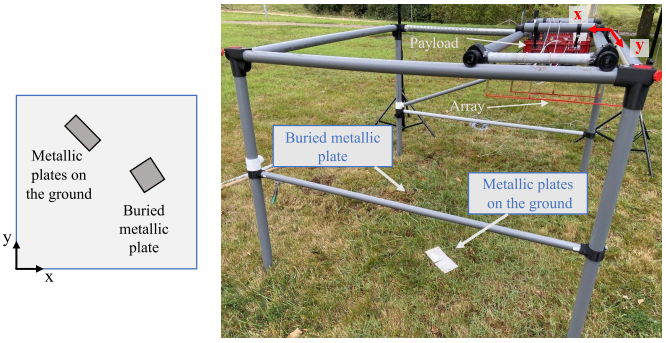

Fig. 10. Portable scanner with the array-based GPR-SAR system and targets used for the experimental validation (two $10\,\text{cm}\times10\,\text{cm}$ metallic plates on the ground and a $16.5\,\text{cm}\times16.5\,\text{cm}$ metallic plate buried at $4\,\text{cm}$ depth).

array, the payload includes the same UWB radar as the one integrated into the UAV, as well as a GNSS-RTK system to provide cm-level accuracy positioning and a microcomputer that gathers all the information and sends the geo-referred radar measurements to a ground control station in real time.

The array-based GPR-SAR system placed in the portable scanner is shown in Fig. 10, together with a scheme of the targets used in the experimental validation. In particular, two metallic plates of $10\,\text{cm}\times10\,\text{cm}$ were placed on the ground, and a square metallic plate of $16.5\,\text{cm}$ side was buried at $4\,\text{cm}$ depth. The schemes analyzed in the theoretical analysis (Section IV) were also compared using the measurements gathered with this portable scanner.

The positions of the center of the array during the measurements performed with the portable setup by moving the sliding arm are depicted in Fig. 11(a)-(d) for the different scanning schemes. As it can be seen, the measurements were not uniformly acquired, in a similar fashion as the data obtained with a UAV-based system. In Fig. 11(e)-(h), the number of samples acquired within each of the cells in which the investigation domain was discretized is depicted. Finally, the sampled cells are depicted in yellow in Fig. 11(i)-(l), whilst non-sampled cells are colored in blue. In agreement with the theoretical analysis presented in Section IV, the schemes U-20 cm and $3X$-40 cm provide the best coverage of the area under inspection (with almost all cells sampled), whereas the scheme U-40 cm gives the worst coverage.

The acquired measurements were processed according to the flowchart explained in Section II, but without applying SVD filtering since in this case there is a target on the ground. The horizontal cuts of the 3D GPR-SAR images at $z = 0\,\text{m}$ and $z = -0.04\,\text{m}$ are shown in Fig. 12 for the different scanning strategies. In the images at $z = 0\,\text{m}$, the metallic plate on the ground can be clearly detected in all cases. In the images at $z = -0.04\,\text{m}$, also for all the considered scanning schemes, the buried metallic plate can be distinguished, as well as a secondary reflection from the target on the ground.

From the analysis of the results depicted in Fig. 12 it is concluded that the schemes U-20 cm and $3X$-40 cm provide GPR-SAR images with better quality (less clutter). Comparing these schemes, it can be observed that the reflection from the buried target (Fig. 12, plane $z = -0.04\,\text{m}$) is slightly more noticeable with the $3X$-40 cm scheme, which could be due to the fact that more measurements are gathered with this scheme. Although with the other two schemes (U-40 cm and $3X$-80 cm) the two targets are still distinguishable, the clutter level is noticeably higher. A high clutter level is especially harmful for the detection of buried targets in those areas where the clutter itself exhibits a significant contrast with the surroundings. These areas are indicated with a red and black ellipse in Fig. 12. In realistic applications, these areas could make the detection of small targets (less than $10\,\text{cm}\times10\,\text{cm}$ size) more difficult and/or they could raise the false alarm rate. Therefore, the former schemes (U-20 cm and $3X$-40 cm) are preferred for the targeted application (landmines and IEDs detection) and they have been selected to continue the experimental validation with the UAV-mounted prototype.

VI. In-flight tests

Finally, flight tests with the UAV prototype were conducted to compare the different scanning strategies for subsurface radar imaging in a realistic scenario. Fig. 13 shows the UAV-mounted array-based GPR-SAR system flying over the inspected scenario. In particular, this validation was performed in the Spanish military training and shooting range "El Palancar", located north of Madrid. The selected area, as well as the position of the targets buried in it, is shown in Fig. 14. In this area, whose size is $4.5\,\text{m}$ across-track $\times\,12\,\text{m}$ along-track, 15 targets of different materials, sizes and composition were buried. The details of these targets are specified in Table II. As shown in this table, these targets included antitank (AT) landmines, antipersonnel (AP) landmines, a pressure plate (PP), an artillery shell, a wooden box, and a plastic jug (acting as IED), among others. The permittivity of the soil has been estimated as $\varepsilon_r \approx 4$ (following the procedure described in [40]). For the plastic targets, the permittivity is expected to be closer to $\varepsilon_r \approx 3$ (in agreement with the dielectric characterization performed in [41] for a small AP mine and with that of most explosives). For the wooden pressure plate (target (iii)), the permittivity is likely to be around $\varepsilon_r \approx 2$ [42].

A. Imaging results

As previously mentioned, the schemes U-20 cm and $3X$-40 cm, which both theoretically provide a 100% coverage of the inspected area (as shown in Section IV), were tested in this scenario. The former required only one flight (composed of 24 along-track sweeps), whereas the latter needed two flights to inspect the whole area (as 36 along-track sweeps must be performed). It is worth noting that without the array, i.e., with a conventional 1 TX-1 RX down-looking GPR (DLGPR) architecture, the number of along-track sweeps drastically increases. Assuming the practical spatial sampling criterion of $\lambda_{min}/2 = 5\,\text{cm}$ (considered for instance in [31]), 91 along-track sweeps would be required to inspect the whole area. In terms of time, the scanning with the uniform strategy (U-20 cm) takes around 10 minutes, whereas the $3X$ approach ($3X$-40 cm) requires 15 minutes for inspecting the

This article has been accepted for publication in IEEE Journal of Selected Topics in Applied Earth Observations and Remote Sensing. This is the author's version which has not been fully edited and content may change prior to final publication. Citation information: DOI 10.1109/JSTARS.2024.3351602

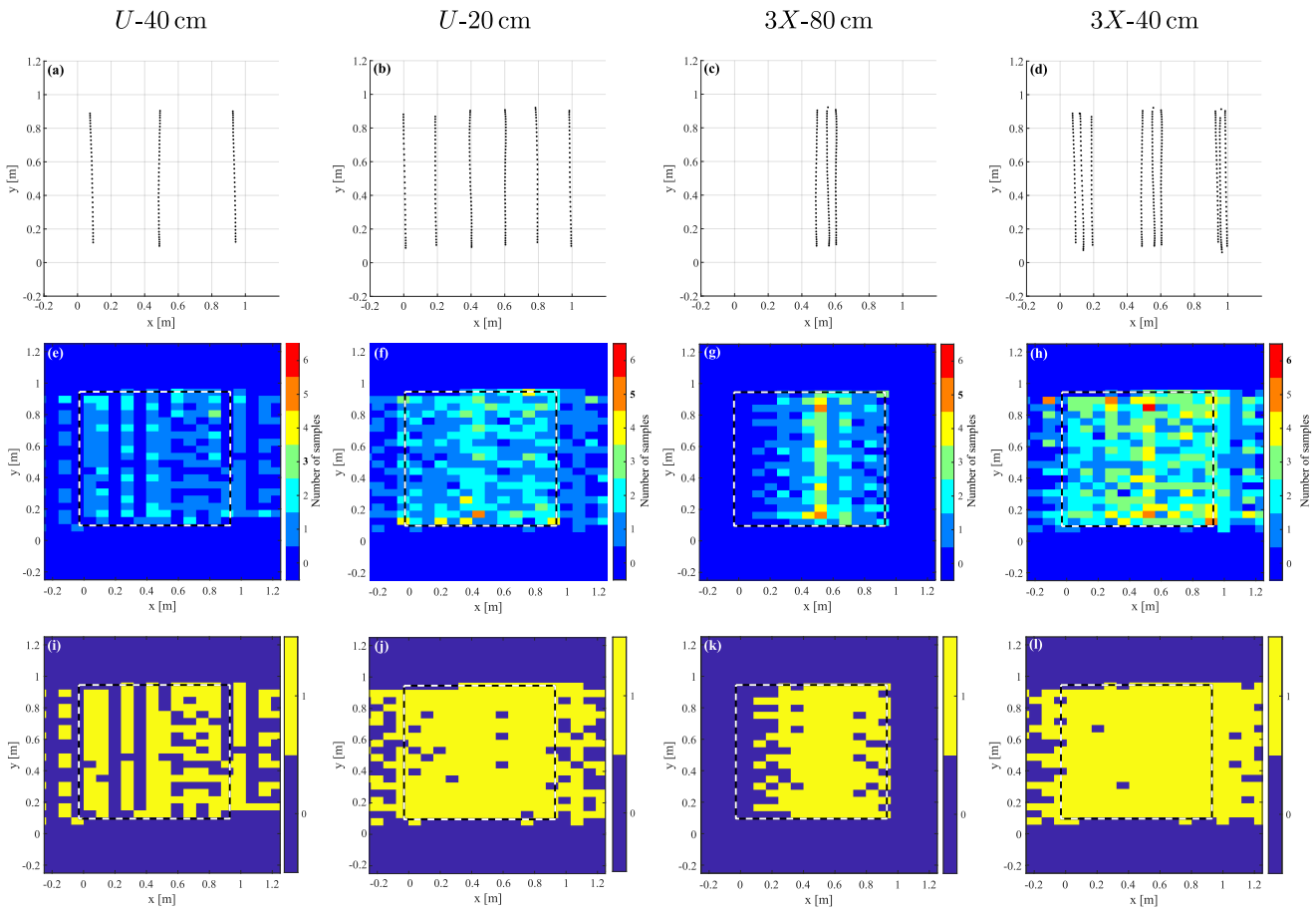

Fig. 11. Measurement positions and sampled cells in the experimental validation performed with the portable scanner. Acquisition schemes: (a,e,i) U-40 cm, (b,f,j) U-20 cm, (c,g,k) $3X$-80 cm, and (d,h,l) $3X$-40 cm. (a-d) Positions of the center of the array during the measurements for the compared acquisition schemes. (e-h) Number of samples per cell in the investigation domain for the corresponding acquisition schemes. (i-l) Sampled cells in the investigation domain in yellow and non-sampled cells in blue. The area under inspection is enclosed by a black and white line in (e-l).

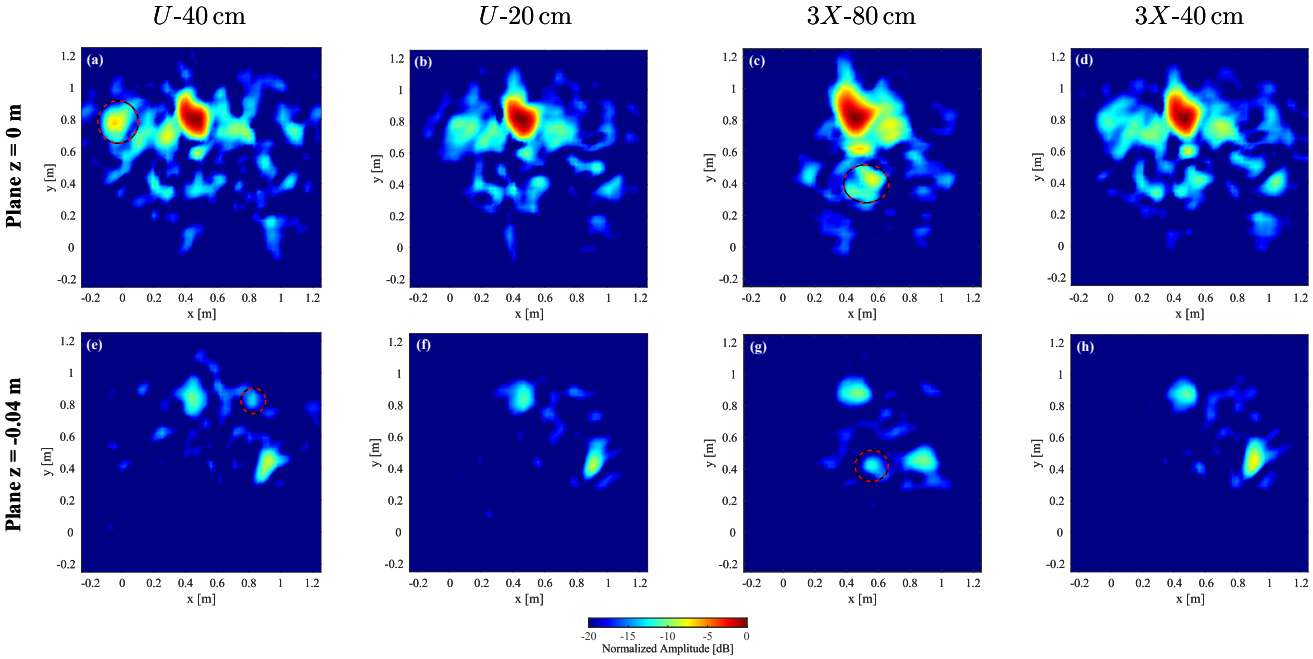

Fig. 12. GPR-SAR images obtained with the array-based GPR-SAR system using a portable scanner (horizontal cuts at $z = 0$ m on the top row, and at $z = -0.04$ m on the bottom row). Scanning strategies compared: (a,e) U-40 cm, (b,f) U-20 cm, (c,g) $3X$-80 cm, and (d,h) $3X$-40 cm. High clutter areas are indicated with a red and black ellipse.

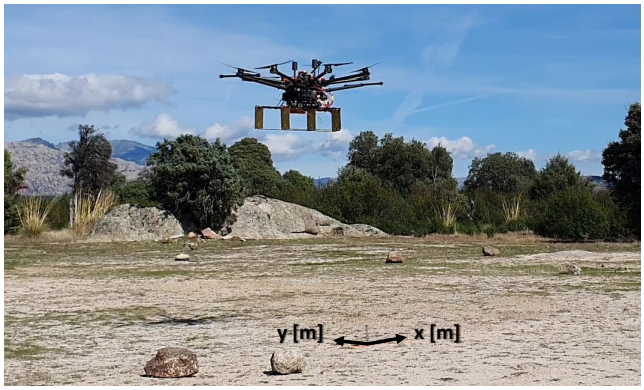

Fig. 13. UAV-mounted array-based GPR-SAR system flying over the inspected area at 1.5 m height.

TABLE II
TARGETS BURIED IN THE VALIDATION SCENARIO FOR IN-FLIGHT TESTS

Target	Type	Size [cm]	Depth(s) [cm]	Composition
(i),(ii), (xi),(xiii)	AT landmine (VS-1.6)	$\varnothing 23 \times 9$ thick	$9, 9, 8, 8$	Plastic
(iii)	Wooden PP	$29 \times 7 \times 4$ thick	≤ 5	Wood
(iv)	Medium AP landmine	$\varnothing 12 \times 5$ thick	≤ 5	Plastic
(v)	Artillery shell	$\varnothing 12 \times 54$ long	14	Plastic
(vi),(xii)	Small AP landmine	$\varnothing 8.5 \times 3$ thick	$\leq 5, \leq 5$	Plastic
(vii)	AP butterfly landmine	$10 \times 4 \times 2$	≤ 5	Plastic
(viii)	AT landmine (square shape)	$35 \times 35 \times 10$	8	Plastic
(ix)	25 litre Jug	$40 \times 28 \times 20$	7	Plastic
(x)	Small water bottle	$\varnothing 8 \times 15$ long	≤ 5	Plastic
(xiv)	Two cans	$10 \times 5 \times 13$	≤ 5	Metallic
(xv)	Wooden box	$35 \times 29 \times 21$	8	Plastic (filled)

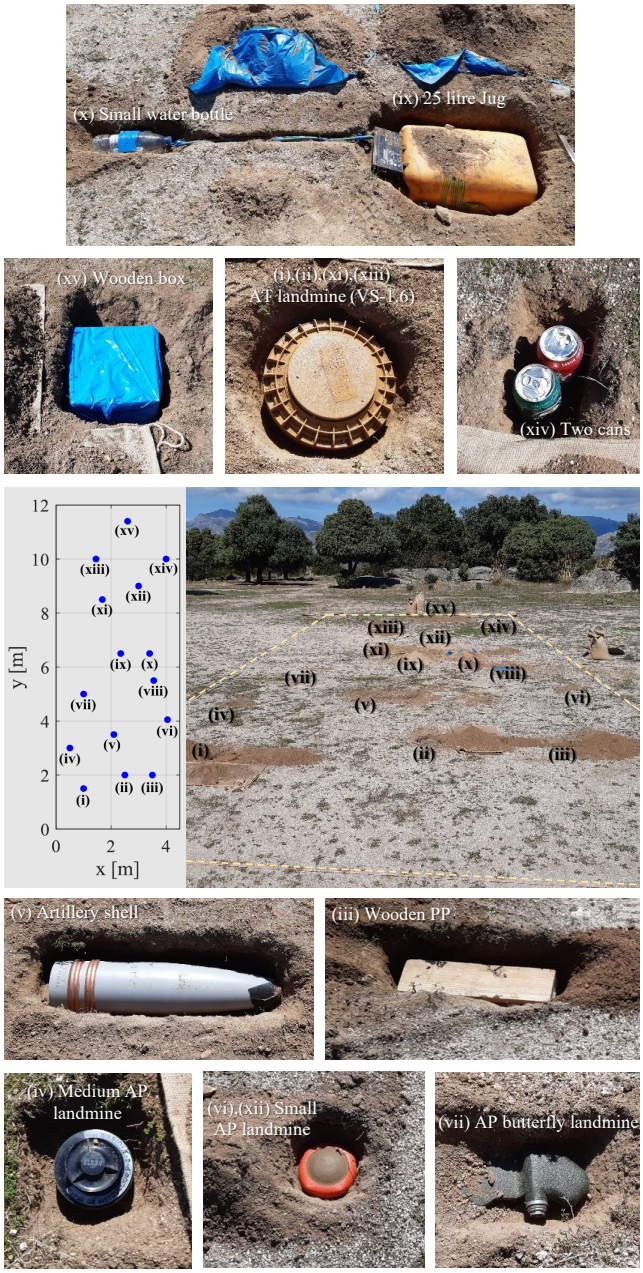

Fig. 14. Picture of the inspected scenario and the buried targets (targets are not shown in scale).

$4.5\,\text{m} \times 12\,\text{m}$ area (plus the time needed to change batteries between the two flights).

The positions of the UAV during the flights, as well as the number of samples and the sampling maps, are shown in Fig. 15 for the compared scanning schemes (U-20 cm on the left and $3X$-40 cm on the right). As shown in Fig. 15(e-f), both schemes provide a good coverage of the inspected $4.5\,\text{m} \times 12\,\text{m}$ area, although the scheme $3X$-40 cm gathers more samples. In particular, 92.7% of the cells within the inspected area (enclosed by a black and white rectangle on Fig. 15 (e-f)) are sampled with this scheme, whereas the coverage decreases to 83.1% with the U-20 cm scheme. A summary of the main statistics for both schemes is given in Table III. In agreement with the results of previous sections, the average of the number of samples per cell is higher with the $3X$-40 cm approach, whereas the standard deviation is smaller for the uniform scheme. The reduction of coverage with respect to the theoretical analysis is mainly due to the deviation of the actual UAV flight path from the predefined one. As the $3X$-40 cm scheme gathers more measurements than the U-20 cm, the reduction in the coverage is smaller for the $3X$-40 cm scheme.

The radar measurements were processed following the flowchart explained in Section II for each scanning strategy. Analyzing the retrieved 3D GPR-SAR images, all targets except target (xii), which is a small AP landmine, were detected with both strategies. Horizontal cuts of these images are shown in Fig. 16 (left column, U-20 cm scheme, and right column, $3X$-40 cm scheme). The targets that are better distinguished are the AT landmines, the wooden PP, the jug and the wooden box, as they exhibit higher reflectivity levels. Besides, both the top and bottom interfaces of these targets

TABLE III
MAIN STATISTICS OF THE NUMBER OF SAMPLES PER CELL, PERCENTAGE OF COVERAGE AND NUMBER OF SWEEPS DURING THE FLIGHTS PERFORMED WITH THE DIFFERENT SCANNING SCHEMES

Scheme	$\overline{N_s}$	σ_{N_s}	Coverage	# Sweeps
U-20 cm	1.43	0.95	83.1%	24
$3X$-40 cm	2.07	1.17	92.7%	36

are detected. The medium-size AP landmines are also clearly distinguishable from the surrounding clutter, whereas only one of the two small-size AP landmines, the one labeled as (vi), is detected.

It should be noted that there are numerous factors that affect the reflectivity levels of the targets and, hence, their detectability. A higher contrast between the permittivity of the targets and the surrounding soil facilitates the detection. The attenuation of the waves increases with the distance but, on the other hand, the detection of shallowly buried targets (at depths ≤ 5 cm) can be challenging (as they might be masked by the clutter from the air-soil interface or their reflection might be mitigated due to the application of clutter removal techniques). In addition, the target characteristics (e.g., shape and size) and the radar system (e.g., frequency, angle of incidence) have also an impact on the detectability. For instance, the shape and composition of the AT landmines (targets (i), (ii), (xi), and (xiii)) and the medium AP landmine (target (iv)) are similar, but the diameter and thickness of the AT landmines are almost twice those of the medium AP landmine. As a result, the AT landmines are better detected than the medium AP landmine, even though they are buried deeper.

By comparing the images of the selected strategies, it can be concluded that the images of the $3X$-40 cm scheme show slightly less clutter than those of the U-20 cm scheme, especially in the layers close to the soil surface ($z \geq -0.05$ m). In addition, the reflectivity levels of the targets detected at deep layers are also higher for the scheme $3X$-40 cm. This can be observed by comparing the reflectivity of the bottom interface of targets (ix) and (xv) at $z = -0.24$ m. Both facts could be explained because with this scheme more measurements are acquired. However, it requires more sweeps (which in turn required two UAV flights for scanning the scenario considered in this section) without having a significant impact on the detection results, as the detected targets are the same as with the U-20 cm scheme.

Besides the visual inspection of the 3D GPR-SAR images, a CFAR algorithm [35] was applied to the horizontal cuts of these images. For both scanning strategies, all targets except targets (x) and (xii) were detected by the CFAR algorithm. Target (x) is the small empty water bottle, which is also hard to distinguish in the radar images (Fig. 16, cut $z = -0.08$ m), whereas target (xii) is the small AP landmine which was also not detected by visual inspection of the SAR image.

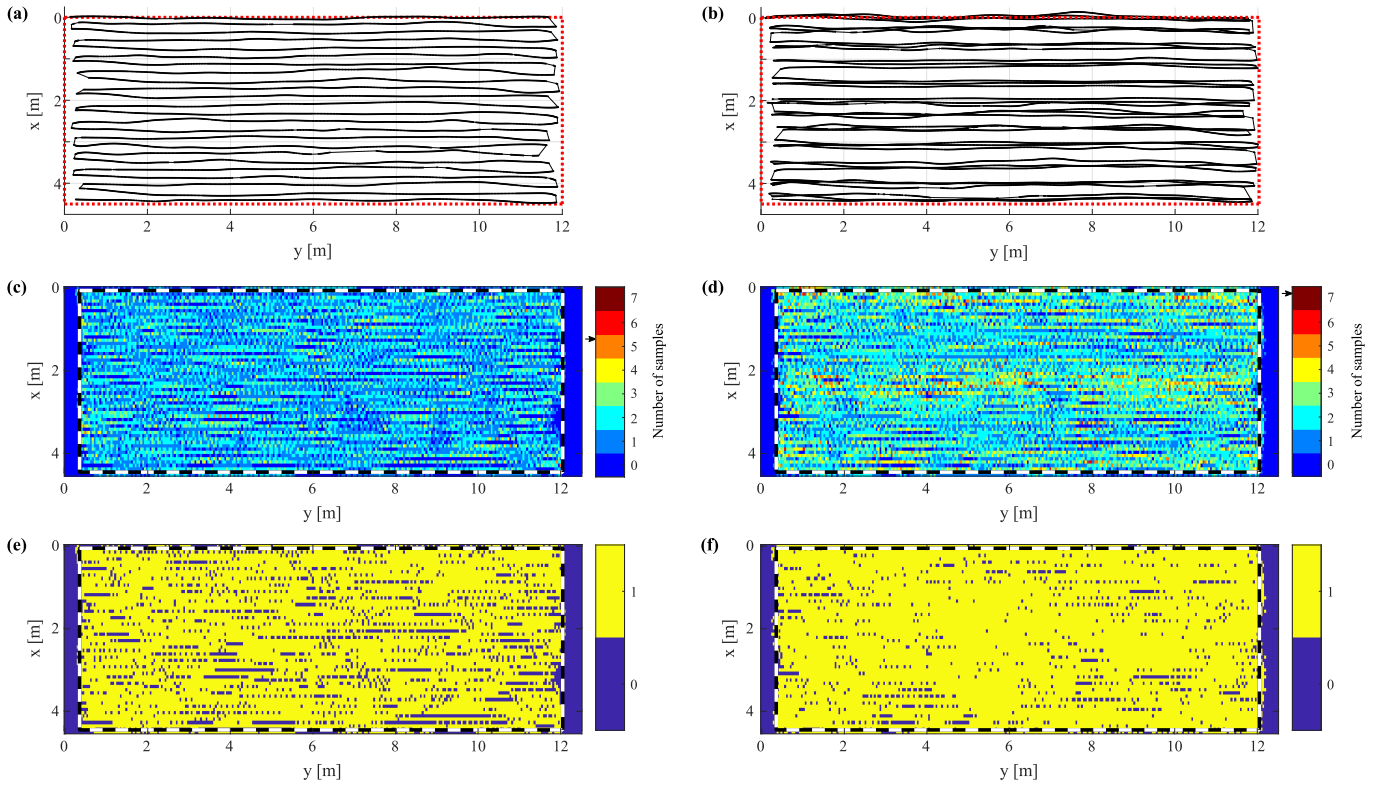

Fig. 15. Measurement positions and sampled cells in the flight tests. Scanning strategies: (a,c,e) U-20 cm, and (b,d,f) $3X$-40 cm. (a-b) Positions of the RTK antenna on board the UAV during the flights. (c-d) Number of samples per cell for the corresponding acquisition schemes (the maximum number of samples per cells for each scheme is indicated with an arrow in the colorbar). (e-f) Sampled cells in yellow and non-sampled cells in blue. The area under inspection is enclosed by a white and black line in (c-f).

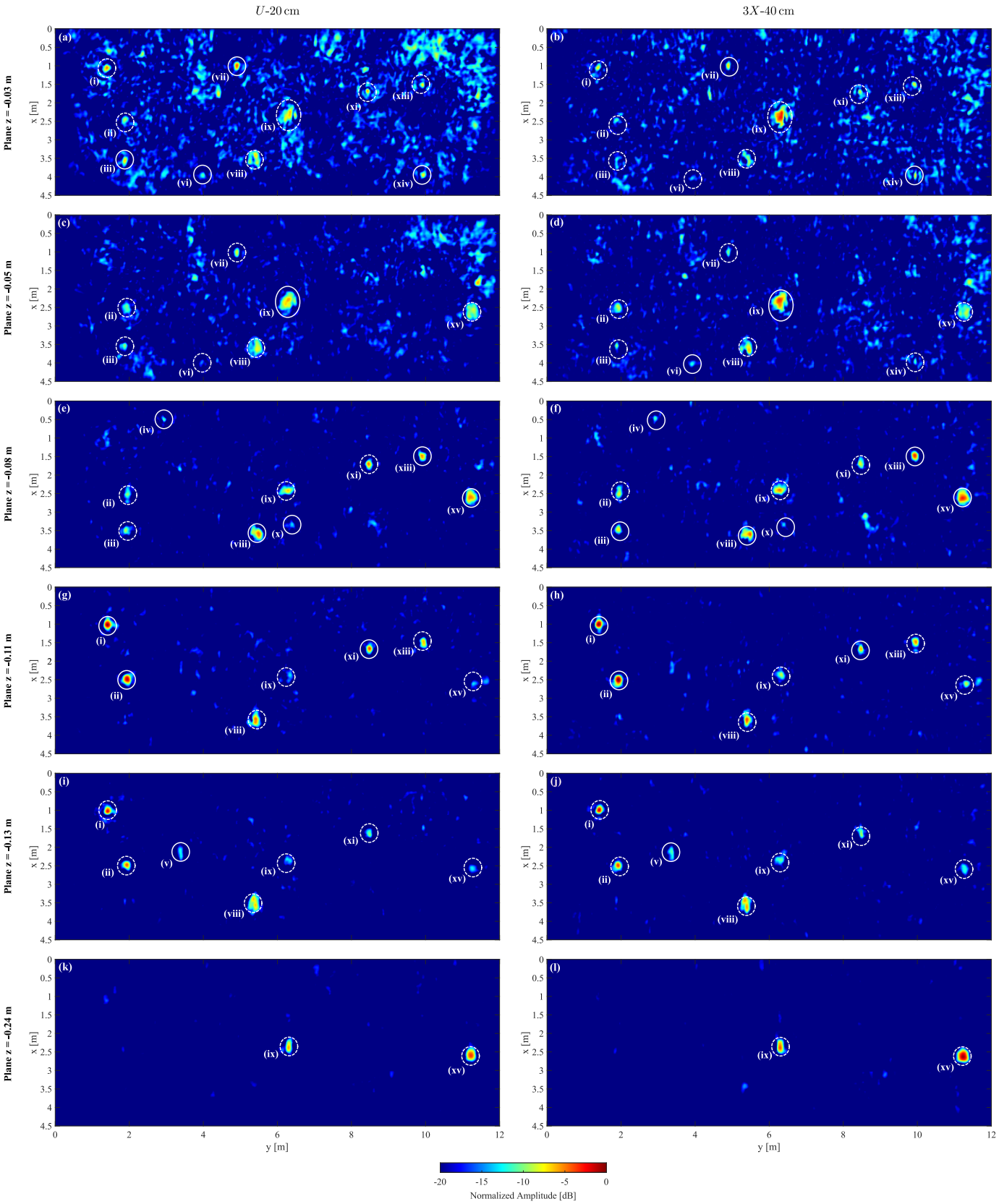

Fig. 16. GPR-SAR images obtained with the array-based GPR-SAR system on board the UAV for the analyzed scanning schemes (U-20 cm on the left and $3X$-40 cm on the right). Horizontal cuts at (a,b) $z = -0.03$ m, (c,d) $z = -0.05$ m, (e,f) $z = -0.08$ m, (g,h) $z = -0.11$ m, (i,j) $z = -0.13$ m, and (k,l) $z = -0.24$ m. Detected targets are surrounded by white ellipses (with a solid line in the layer where the top or main interface of each target is better detected).

B. Assessment of sparse schemes

Although only the U-20 cm and $3X$-40 cm schemes have been selected to perform the flight tests (since they are the ones that theoretically guarantee a full coverage of the investigation domain, as analyzed in Section IV), it is also of interest to assess how the sparser U-40 cm and $3X$-80 cm schemes would perform during flights. For this purpose, half of the sweeps of the original flights (U-20 cm and $3X$-40 cm schemes) have been selected to synthesize the U-40 cm and $3X$-80 cm schemes, respectively. The forward sweeps of U-20 cm yield the scheme U-40 cm FW, and the backward sweeps yield U-40 cm BW. Half of the sweeps of $3X$-40 cm are used to obtain $3X$-80 cm (A) (when starting with the first along-track sweep) and $3X$-80 cm (B) (when starting with the fourth along-track sweep). As can be observed in Fig. 17, the clutter level in the radar images increases when considering the U-40 cm and $3X$-80 cm schemes compared to the results obtained with the original flights.

To compare all the schemes, four targets have been selected: the bottom of the wooden box (xv), one AT landmine (i), the AP butterfly landmine (vii) and a small AP landmine (vi). The radar images corresponding to these targets are shown in Fig. 17, where each row corresponds to one target and each column to one sampling scheme. Medium and big-size targets (e.g., the wooden box and the AT landmine) are still clearly detected using the sparser schemes (U-40 cm and $3X$-80 cm), although the shape is not so well reconstructed. The AP butterfly landmine is also detected with the sparser schemes, but it becomes more evident that the signal to clutter ratio worsens compared to the results obtained with the original schemes (U-20 cm and $3X$-40 cm). Finally, the smallest AP landmine cannot be detected with any of the sparse schemes except $3X$-80 cm (A). This is because in the case of U-40 cm schemes the clutter level is similar to the target reflectivity, and for the $3X$-80 cm (B) scheme the region around the target is significantly worse sampled than for $3X$-80 cm (A). Therefore, it can be concluded that if the goal is to detect only medium to big size targets, the sparser schemes (U-40 cm and $3X$-80 cm) can be used to reduce the inspection time even further (in particular, by half the time needed for the original schemes).

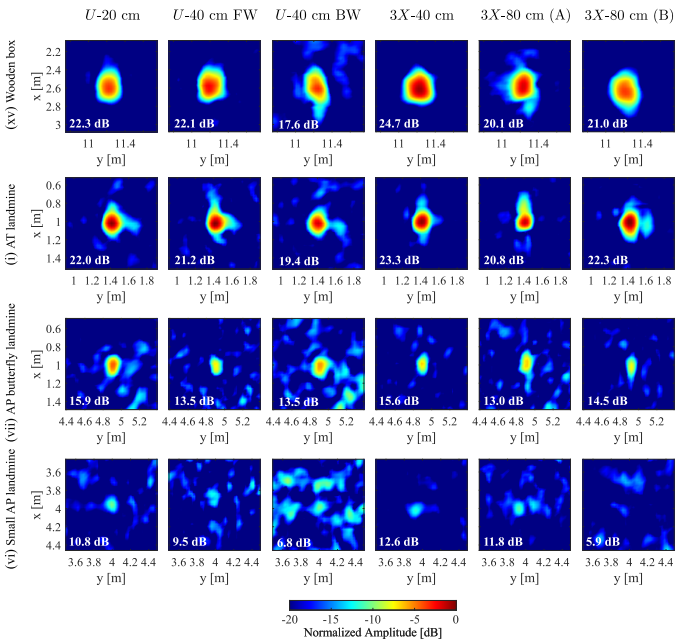

Fig. 17. GPR-SAR images obtained with the array-based GPR-SAR system on board the UAV for several targets (by rows, the wooden box, an AT landmine, the AP butterfly landmine and a small AP landmine) and for different scanning schemes (by columns, U-20 cm, U-40 cm FW, U-40 cm BW, $3X$-40 cm, $3X$-80 cm (A) and $3X$-80 cm (B)). The PSCR is indicated in white for each case.

C. Discussion

In Subsection VI-A, the selected scanning schemes ($3X-40$ cm and $U-20$ cm) have been compared mainly qualitatively, by visually inspecting the retrieved radar images. This comparison allowed to conclude that the same targets are detected with both schemes, although the scheme $3X-40$ cm provides in general better imaging results (e.g., less clutter particularly in the layers close to the soil surface, or higher reflectivity for the deepest targets) at the expense of requiring a longer flight time.

For quantitatively comparing the imaging results, a metric called Peak Signal to Clutter Ratio (PSCR) has been employed. The PSCR is defined, for each target, as follows:

$$\text{PSCR [dB]} = 10\log_{10}\left(\frac{\max_{x,y\in A_t}|\boldsymbol{\rho}(x,y,z_t)|^2}{\frac{1}{N_c}\sum_{x,y\in A_c}|\boldsymbol{\rho}(x,y,z_t)|^2}\right), \quad (4)$$

where $\boldsymbol{\rho}(x,y,z_t)$ is the reflectivity (i.e., the radar image) in the slice $z=z_t$ (where the target is located), A_t and A_c are the target and clutter regions (i.e., the pixels corresponding to the target and to the clutter, respectively), and N_c is the number of pixels belonging to the clutter area. For the computation of the PSCR, the clutter region is restricted to an area of $1\,\text{m}\times 1\,\text{m}$ centered at the target position (as displayed in Fig. 17), as the key to detect the targets is to distinguish them from the surrounding clutter. The target region, A_t, is defined (for each target) as a rectangle centered at the target position which encloses the whole target (according to the size of the target given in Table II).

The PSCR has been computed for all buried targets and, in the case of the biggest targets (square shape AT landmine, jug and wooden box) the PSCR corresponding to both the top and bottom interfaces has been considered. For most targets (in particular, more than 80%), the PSCR values are higher for the $3X-40$ cm scheme than for the $U-20$ cm, in agreement with the conclusion achieved by visually inspecting the GPR-SAR images. On average, there is a 1 dB improvement in the PSCR when using the $3X-40$ cm scheme. As an example, for the AT landmine (target (i)), depicted in the second row of Fig. 17, the PSCR for the $3X-40$ cm strategy is 23.3 dB, whereas for the $U-20$ cm strategy it decreases to 22.0 dB (i.e., there is 1.3 dB difference). In the case of the bottom of the wooden box (target (xv)), the improvement in the PSCR for the $3X-40$ cm scheme is higher (2.4 dB difference), as expected from the increase in the target reflectivity observed in the GPR-SAR images (see first row of Fig. 17).

In Subsection VI-B, the performance of the sparse schemes ($3X-80$ cm and $U-40$ cm) was analyzed, concluding that

TABLE IV
COMPARISON OF THE PERFORMANCE OF THE SCANNING SCHEMES DURING FLIGHT TESTS (WHEN INSPECTING AN AREA OF $4.5\,\mathrm{m} \times 12\,\mathrm{m}$)

Scheme	$\overline{\mathrm{PSCR}}$ [dB]	Flight time [min]	Remarks
U-20 cm	16.7	10	Detailed mapping, higher speed
$3X$-40 cm	17.7	15	Detailed mapping, better results
U-40 cm	14.6	5	Fastest inspection, mid-big targets
$3X$-80 cm	15.3	7.5	Rapid inspection, mid-big targets

medium to big size targets are still clearly distinguishable although the quality of the GPR-SAR images worsens. This is also in agreement with the behavior observed for the PSCR values. For instance, for the AP butterfly landmine (target (vii), third row of Fig. 17), the PSCR for the $3X-40$ cm scheme is 15.6 dB (decreasing to 13.0 dB and 14.5 dB for $3X-80$ cm (A) and (B), respectively), whereas for U-20 cm is 15.9 dB (decreasing to 13.5 dB for $U-40$ cm FW and BW). In the case of the small AP mine (target (vi), fourth row of Fig. 17), the PSCR for $3X-40$ cm is 12.6 dB and it worsens slightly to 11.8 dB for $3X-80$ cm (A). However, for the $3X-80$ cm (B) the PSCR drops to 5.9 dB because, as previously mentioned, the area around the target is worse sampled than for the $3X-80$ cm (A).

The performance of the scanning schemes during the flight tests (when inspecting an area of $4.5\,\mathrm{m} \times 12\,\mathrm{m}$) is summarized in Table IV, where the average PSCR and the required flight time for each scheme are displayed. As can be observed, the highest PSCR is obtained for the $3X-40$ cm scheme. The $U-20$ cm scheme yields similar performance as $3X-40$ cm (only 1 dB difference in the PSCR), whilst the sparse schemes present lower PSCR values. In contrast, the sparse schemes require significantly shorter flight times than the $3X-40$ cm and the $U-20$ cm schemes to inspect a given area. These results are in agreement with the previous discussion from a qualitative point of view, showing that a trade-off between imaging performance (image quality/detectability of small targets) and flight time must be established when choosing a given scanning scheme. In particular, in a context where the detection of small targets is crucial and/or detailed mapping is desired, the dense schemes should be prioritized at the expense of longer flight times ($U-20$ cm for achieving a higher inspection speed or $3X-40$ cm for better imaging results). In contrast, the sparse schemes can be of interest in applications involving the detection of medium to large size targets when a fast survey speed is required (with $U-40$ cm providing the fastest inspection).

VII. CONCLUSION

This article has analyzed several scanning strategies to increase the scanning throughput of an array-based GPR-SAR system on board a UAV. In particular, two different strategies have been compared: a uniform scheme (where the sweeps are separated a given distance) and a non-uniform strategy called $3X$ (which aims to minimize the presence of grating lobes and to achieve a uniform illumination in the area under the array). Both strategies have been analyzed following a theoretical analysis (proving that a 100% coverage of the investigation domain can be achieved) and with experiments (both on ground and in-flight).

Results show that the same targets can be detected with both (dense) scanning schemes (i.e., U-20 cm and $3X$-40 cm). The latter scheme ($3X$-40 cm) yields radar images with slightly less clutter (especially at shallow layers) and, furthermore, the deepest targets exhibit higher signal levels. However, it requires more sweeps than the uniform approach (U-20 cm) and it is not as easy to implement (as a UAV mission control software must be developed to define such a non-uniform flight path). It has also been shown that the sparser schemes (U-40 cm and $3X$-80 cm) could also be used if the goal is to detect medium to big size targets. In the case of the uniform sparse scheme (U-40 cm), only 5 minutes would be needed to inspect an area of $60\,\mathrm{m}^2$, further increasing the survey speed of the system.

Taking into account the above considerations, for detailed mapping the dense scanning schemes (U-20 cm and $3X$-40 cm) should be used. In particular, to obtain better signal to clutter levels, the scheme $3X$-40 cm is beneficial, at the expense of longer flights. Alternatively, if the goal is to reduce the inspection time (without jeopardizing the detection of the targets), the U-20 cm should be employed. Moreover, the inspection time can be furthered decreased (leveraging the sparse U-40 cm or $3X$-80 cm schemes) if only the detection of medium to large targets is required.

Compared to the conventional single-channel DLGPR architecture, using the array-based GPR-SAR system results in a drastic reduction on the number of required sweeps to inspect a given area. In particular, to inspect an area of $4.5\,\mathrm{m} \times 12\,\mathrm{m}$ only $39.6\,\%$ of the sweeps needed with a conventional single-channel DLGPR architecture are required with the $3X$-40 cm scheme, and only $26.4\,\%$ with the uniform strategy (U-20 cm). This means that the (dense) uniform strategy would allow to inspect an area of $60\,\mathrm{m}^2$ in around 10 minutes without jeopardizing the detection capabilities. This constitutes a significant improvement, paving the way to the operational use of this technology.

ACKNOWLEDGMENTS

The authors would like to thank the personnel of the Counter Improvised Explosive Devices Center of Excellence (C-IED CoE) and the Ministry of Defense of Spain for their counseling and support on the topic of landmine and IED detection, as well as for the preparation of the scenarios for the flight tests.

REFERENCES

[1] Y. Alvarez Lopez, M. Garcia-Fernandez, G. Alvarez-Narciandi, and F. Las-Heras Andres, "Unmanned aerial vehicle-based ground-penetrating radar systems: A review," *IEEE Geoscience and Remote Sensing Magazine*, pp. 2–22, 2022.

[2] H. Jol, *Ground Penetrating Radar: Theory and Applications*. Amsterdam: Elsevier Science, 2008.

[3] M. Garcia-Fernandez, Y. Alvarez-Lopez, A. Arboleya-Arboleya, B. Gonzalez-Valdes, Y. Rodriguez-Vaqueiro, F. Las-Heras, and A. Pino-Garcia, "Synthetic aperture radar imaging system for landmine detection using a ground penetrating radar on board a unmanned aerial vehicle," *IEEE Access*, vol. 6, pp. 45 100–45 112, 2018.

[4] B. Gonzalez, Y. Alvarez, A. Arboleya, Y. R. Vaqueiro, M. Garcia, F. Las-Heras, and A. G. Pino, "Airborne systems and detection methods localization and production of images of buried objects and characterization of the composition of the subsurface," 7 2017, patents ES2577403B2, EP3407007B1, CN109073348B, US10895636B2. [Online]. Available: https://patents.google.com/patent/WO2017125627A1/en

[5] M. Schartel, R. Burry, R. Bahnemannz, W. Mayer, , and C. Waldschmidt, "An experimental study on airborne landmine detection using a circular synthetic aperture radar," 2020. [Online]. Available: https://arxiv.org/abs/2005.02600

[6] J. Colorado, M. Perez, I. Mondragon, D. Mendez, C. Parra, C. Devia, J. Martinez-Moritz, and L. Neira, "An integrated aerial system for landmine detection: SDR-based ground penetrating radar onboard an autonomous drone," *Advanced Robotics*, vol. 31, pp. 791–808, 2017.

[7] M. R. P. Cerquera, J. D. C. Montaño, and I. Mondragon, "UAV for Landmine Detection Using SDR-Based GPR Technology," in *Robots Operating in Hazardous Environments*, H. Canbolat, Ed. Rijeka: IntechOpen, 2017, ch. 2.

[8] K. Wu, G. A. Rodriguez, M. Zajc, E. Jacquemin, M. Clément, A. De Coster, and S. Lambot, "A new drone-borne GPR for soil moisture mapping," *Remote Sensing of Environment*, vol. 235, p. 111456, 2019.

[9] R. O. R. Jenssen, M. Eckerstorfer, and S. Jacobsen, "Drone-mounted ultrawideband radar for retrieval of snowpack properties," *IEEE Transactions on Instrumentation and Measurement*, vol. 69, no. 1, pp. 221–230, 2020.

[10] J. Lopez-Sanchez and J. Fortuny-Guasch, "3-D radar imaging using range migration techniques," *IEEE Transactions on Antennas and Propagation*, vol. 48, no. 5, pp. 728–737, 2000.

[11] J. Schorlemer, J. Jebramcik, I. Rolfes, and J. Barowski, "Comparison of Short-Range SAR Imaging Algorithms for the Detection of Landmines using Numerical Simulations," in *2021 18th European Radar Conference (EuRAD)*, 2022, pp. 393–396.

[12] R. Solimene, F. Soldovieri, G. Prisco, and R. Pierri, "Three-dimensional microwave tomography by a 2-D slice-based reconstruction algorithm," *IEEE Geoscience and Remote Sensing Letters*, vol. 4, no. 4, pp. 556–560, 2007.

[13] C. Noviello, G. Esposito, I. Catapano, and F. Soldovieri, "Multilines imaging approach for mini-UAV radar imaging system," *IEEE Geoscience and Remote Sensing Letters*, vol. 19, 2022.

[14] M. Gonzalez-Diaz, M. Garcia-Fernandez, Y. Alvarez-Lopez, and F. Las-Heras, "Improvement of GPR SAR-based techniques for accurate detection and imaging of buried objects," *IEEE Transactions on Instrumentation and measurement*, vol. 6, pp. 3126–3138, 2020.

[15] M. García-Fernández, G. Álvarez Narciandi, Y. Álvarez López, and F. Las-Heras Andrés, "Improvements in GPR-SAR imaging focusing and detection capabilities of UAV-mounted GPR systems," *ISPRS Journal of Photogrammetry and Remote Sensing*, vol. 189, pp. 128–142, 2022.

[16] R. Burr, M. Schartel, A. Grathwohl, W. Mayer, T. Walter, and C. Waldschmidt, "UAV-borne FMCW InSAR for focusing buried objects," *IEEE Geoscience and Remote Sensing Letters*, pp. 1–5, 2021.

[17] X. Feng, M. Sato, Y. Zhang, C. Liu, F. Shi, and Y. Zhao, "CMP Antenna Array GPR and Signal-to-Clutter Ratio Improvement," *IEEE Geoscience and Remote Sensing Letters*, vol. 6, no. 1, pp. 23–27, 2009.

[18] E. Schreiber, M. Peichl, A. Heinzel, S. Dill, F. Bischeltsrieder, S. Anger, T. Kempf, and M. Jirousek, "Challenges for operational use of ground-based high-resolution SAR for landmines and UXO detection," in *Proceedings of EUSAR 2016: 11th European Conference on Synthetic Aperture Radar*, 2016, pp. 1–4.

[19] E. Schreiber, M. Peichl, S. Dill, S. Anger, A. Heinzel, F. Bischeltsrieder, T. Kempf, and M. Jirousek, "Theoretical and experimental investigations of a ground-based high-resolution SAR for buried object detection," in *2015 European Radar Conference (EuRAD)*, 2015, pp. 229–232.

[20] M. Peichl, E. Schreiber, A. Heinzel, and S. Dill, "Novel Imaging Radar Technology for Detection of Landmines and Other Unexploded Ordnance," *European Journal for Security Research*, vol. 2, pp. 23–37, 2017.

[21] J. Leckebusch, "Test and data processing of a stepped-frequency GPR array," *ArcheoSciences, revue d'archéométrie*, vol. 33, pp. 305–307, 2009.

[22] A. Srivastav, P. Nguyen, M. McConnell, K. A. Loparo, and S. Mandal, "A highly digital multiantenna ground-penetrating radar (GPR) system," *IEEE Transactions on Instrumentation and Measurement*, vol. 69, no. 10, pp. 7422–7436, 2020.

[23] M. Garcia-Fernandez, Y. Alvarez-Lopez, and F. Las-Heras, "Airborne multi-channel ground penetrating radar for improvised explosive devices and landmine detection," *IEEE Access*, vol. 8, pp. 165 927–165 943, 2020.

[24] C. Roussi, I. Xique, J. Burns, and B. Hart, "Buried object imaging using a small UAS-based GPR," in *Proceedings of the SPIE 11012, Detection and Sensing of Mines, Explosive Objects, and Obscured Targets XXIV*, vol. 11012, 2019, pp. 1–9.

[25] M. García-Fernández, G. Álvarez Narciandi, Y. Álvarez López, and F. Las-Heras Andrés, "Array-based Ground Penetrating Synthetic Aperture Radar on board an Unmanned Aerial Vehicle for enhanced buried threats detection," *IEEE Transactions on Geoscience and Remote Sensing*, vol. 61, 2023.

[26] Z. Sun, J. Wu, G. G. Yen, Z. Lu, and J. Yang, "Performance analysis and system implementation for energy-efficient passive UAV radar imaging system," *IEEE Transactions on Vehicular Technology*, vol. 72, pp. 9938–9955, 2023.

[27] A. Savkin, W. Ni, and M. Eskandari, "Effective UAV navigation for cellular-assisted radio sensing, imaging, and tracking," *IEEE Transactions on Vehicular Technology*, 2023 (Early Access).

[28] M. Garcia-Fernandez, Y. Alvarez-Lopez, B. Gonzalez-Valdes, Y. Rodriguez-Vaqueiro, A. Arboleya-Arboleya, and F. L. Heras, "Recent advances in high-resolution ground penetrating radar on board an unmanned aerial vehicle," in *2019 13th European Conference on Antennas and Propagation (EuCAP)*, 2019, pp. 1–5.

[29] M. Garcia-Fernandez, Y. Alvarez-Lopez, and F. Las Heras, "Autonomous airborne 3D SAR imaging system for subsurface sensing: UWB-GPR on board a UAV for landmine and IED detection," *Remote Sensing*, vol. 11, no. 20, 2019.

[30] Y. Rodriguez-Vaqueiro, J. Vázquez-Cabo, B. Gonzalez-Valdes, A. Pino, Y. Álvarez, M. Garcia-Fernandez, F. Las-Heras, and A. Arboleya, "Array of Antennas for a GPR system onboard a UAV," in *2019 IEEE International Symposium on Antennas and Propagation and USNC-URSI Radio Science Meeting*, 2019, pp. 821–822.

[31] M. García Fernández, G. Álvarez Narciandi, A. Arboleya, C. Vázquez Antuña, F. L.-H. Andrés, and Y. Álvarez López, "Development of an Airborne-Based GPR System for Landmine and IED Detection: Antenna Analysis and Intercomparison," *IEEE Access*, vol. 9, pp. 127 382–127 396, 2021.

[32] M. E. Yanik and M. Torlak, "Near-Field MIMO-SAR Millimeter-Wave Imaging With Sparsely Sampled Aperture Data," *IEEE Access*, vol. 7, pp. 31 801–31 819, 2019.

[33] M. Garcia Fernandez, Y. Alvarez Lopez, B. Gonzalez-Valdes, A. Arboleya Arboleya, Y. Rodriguez Vaqueiro, F. Las-Heras Andres, and A. Pino Garcia, "UAV-mounted GPR for NDT applications," in *2018 15th European Radar Conference (EuRAD)*, 2018, pp. 2–5.

[34] C. Rappaport, M. El-Shenawee, and H. Zhan, "Suppressing GPR Clutter from Randomly Rough Ground Surfaces to Enhance Nonmetallic Mine Detection," *Subsurface Sensing Technologies and Applications*, vol. 4, pp. 311–326, 2003.

[35] J. D. Taylorl, *Advanced Ultrawideband Radar: Signals, Targets, and Applications*. Boca Raton, USA: CRC Press, Tayor and Francis Group, 2019.

[36] M. Garcia-Fernandez, G. Alvarez-Narciandi, Y. Alvarez-Lopez, and F. Las-Heras, "Comparison of subsampling strategies for UAV-mounted subsurface radar imaging systems," in *2022 IEEE AP-S Symposium on Antennas and Propagation*, 2022.

[37] D. Sheen, D. McMakin, and T. Hall, "Three-dimensional millimeter-wave imaging for concealed weapon detection," *IEEE Transactions on Microwave Theory and Techniques*, vol. 49, no. 9, pp. 1581–1592, 2001.

[38] E. M. Johansson and J. E. Mast, "Three-dimensional ground-penetrating radar imaging using synthetic aperture time-domain focusing," in *Advanced Microwave and Millimeter-Wave Detectors*, S. S. Udpa and H. C. Han, Eds., vol. 2275, International Society for Optics and Photonics. SPIE, 1994, pp. 205 – 214.

[39] M. García-Fernández, Y. Álvarez López, A. De Mitri, D. Castrillo Martínez, G. Álvarez Narciandi, and F. Las-Heras Andrés, "Portable and Easily-Deployable Air-Launched GPR Scanner," *Remote Sensing*, vol. 12, no. 11, 2020.

[40] Y. Alvarez Lopez, M. Garcia Fernandez, A. Arboleya Arboleya, B. Gonzalez-Valdes, Y. Rodriguez Vaqueiro, F. Las-Heras Andres, and A. Pino Garcia, "SAR-based technique for soil permittivity estimation," *International Journal of Remote Sensing*, vol. 38, no. 18, pp. 5168–5185, 2017.

[41] F. Lombardi, H. Griffiths, L. Wright, and A. Balleri, "Dependence of landmine radar signature on aspect angle," *IET Radar Sonar Navigation*, vol. 11, pp. 892–902, 2017.
[42] S. Kol, "Pine thermal, dielectric properties," *BioResources*, vol. 4, no. 4, pp. 1663–1669, 2009.